Earth ArXiv

This is a non-peer-reviewed preprint submitted to EarthArXiv.

Please note the manuscript has yet to be formally accepted for publication. Subsequent versions of this manuscript may have slightly different content. If accepted, the final version of this manuscript will be available via the 'Peer-reviewed Publication DOI' link on the right-hand side of this webpage. Please feel free to contact any of the authors; we welcome feedback.

A simple model for wind-driven ocean circulation in unbounded domains

Xinyi Meng*[1] and Esteban G. Tabak[1]

[1]Courant Institute of Mathematical Sciences, New York University, New York, USA

April 8, 2026

Abstract

An idealized barotropic model satisfying a Stommel–type vorticity balance is formulated for wind–driven circulation in a zonally unbounded channel with spatially varying bottom drag, motivated by the Antarctic Circumpolar Current through Drake Passage. An explicit solution is obtained in the high–drag passage and a Sverdrup interior with western boundary layer is derived in the weak–drag basin; the solutions are matched by continuity of streamfunction and flux. The model provides a simple qualitative explanation for the emergence of a northward Malvinas Current branch when the Antarctic Circumpolar Current crosses the Drake Passage.

Index terms — Stommel's model, wind-driven circulation, geophysical fluid dynamics.

1 Introduction

Wind–driven ocean circulation has long been understood through a balance between planetary vorticity input by the wind and its removal by friction and lateral transport. In the classical barotropic view, a large-scale curl of the wind stress creates a meridional equator-ward Sverdrup interior flow, which returns through narrow western boundary currents, described by Stommel's model and its extensions to more realistic geometries and stratification [1, 2]. While these idealized gyre theories were developed primarily for closed ocean basins, the core components, β–plane vorticity balance, bottom friction, and lateral boundaries, are also fundamental to theories of zonally unbounded currents. In the Southern Ocean, the Antarctic Circumpolar Current (ACC) flows through Drake Passage, a narrow constriction of the circumpolar current that links all major ocean basins. The transport of the ACC through the Drake Passage significantly influences the exchange of heat, freshwater, and tracers between basins. As a result, the transport of the ACC through Drake Passage plays a central role in the global circulation. It provides the continuous pathway by which water masses can circle the globe, and its volume transport is remarkably large: repeat hydrographic sections along the World Ocean Circulation Experiment (WOCE) SR1b line across Drake Passage give time-mean baroclinic transports of about 135 Sv relative to deep reference levels [3], inverse estimates that combine moored current meters with satellite altimetry yield full-depth transports of about 141 ± 3 Sv with a standard deviation of order 10 Sv [4], and a $1/12°$ eddy-resolving global ocean model produces a mean Drake Passage transport of ~ 157 Sv, roughly midway between these

---

[*] Email: xm2406@nyu.edu

observational estimates [5]. Those results identify the importance of ACC in the global circulation development, and the Drake Passage as a choke point for ACC, where relatively small changes in local dynamics can project onto basin-scale dynamics.

Drake Passage concentrates several ACC jets and multiple hydrographic fronts into a relatively narrow meridional band. This compression sharpens horizontal gradients and increases vertical shear, preconditioning the flow for baroclinic instability and vigorous mesoscale eddy generation. Observational syntheses and front climatologies show closely spaced ACC fronts and strong jets crossing the Passage[6, 7]. In addition, turbulence and diapycnal mixing are locally enhanced in Drake Passage compared to surrounding sectors of the Southern Ocean [8]. In this setting, transient eddies and standing meanders continually extract available potential energy from strongly steep isopycnals, maintaining a saturated, highly turbulent state. These dynamical features make the Passage an outlier in terms of both eddy activity and mixing compared to other open ACC sectors. In other words, the Passage adds geometric complexity. It introduces mean momentum into turbulent and wave motions. These changes appear on a large scale as increased effective bottom drag.

Most recent theoretical studies of the ACC passing through Drake Passage employ highly idealized barotropic channel models with uniform friction or depend on numerical simulations that resolve baroclinic eddies and complex topography [5, 9]. On the other hand, high–resolution primitive–equation models in realistic settings demonstrate how small–scale abyssal hills and rough ridges generate topographic form stress and standing waves [10]. What is missing is a simple, fully analytic model that focuses on the dynamical role of a narrow region of enhanced bottom drag embedded in a channel that is otherwise only weakly dissipative. The goal of this paper is to fill that gap using the simplest possible extension of Stommel's barotropic model to a zonally unbounded channel with a partial ridge. We consider a β–plane channel that is periodic in the zonal direction and bounded meridionally, with a shallow strip representing the high bottom drag region caused by the narrow passage and significant uneven bottom topography, and a deeper basin on its eastern side. This configuration provides a minimal barotropic analogue of an ACC segment intersecting a narrow, high-drag passage adjacent to a weak-drag basin, reminiscent of Drake Passage and the Malvinas Current system.

The paper is organized as follows: In Section 2, we introduce the theoretical model, including the idealized topographic configuration, the governing Stommel–type vorticity balance, and the decomposition into a high–drag mountain strip and a weak–drag basin. We derive an explicit solution about the passage and a solution consisting of an inner flow and a boundary layer in the larger basin. Appropriate matching conditions between two regions are discussed. Then, based on the ERA5 dataset we estimate the wind stress parameters. Section 3 discusses the dynamical implications of the solution, emphasizing how drag heterogeneity and the presence of a narrow high–drag passage can rotate part of the wind–driven transport into a meridional branch reminiscent of the Malvinas Current. Section 4 summarizes the main results and outlines possible extensions, including more realistic boundary conditions and baroclinic generalizations.

2 Theoretical model

2.1 Model Setup

We consider a barotropic, wind–driven flow in a periodic channel with a partial topographic ridge representing an undersea mountain. The horizontal domain is $D = [-x_0, L_x] \times [0, L_y]$, where $y = 0$ and $y = L_y$ indicate the southern and northern boundaries, respectively. The topographic ridge spans the strip $x \in [-x_0, 0]$, and its height $h(x)$ jumps from 0 to a constant value h_m, so that the local depth in the entire domain D is given by

$$H(x) = \begin{cases} H_0, & x \in [0, L_x], \\ H_0 - h_m, & x \in [-x_0, 0], \end{cases} \tag{1}$$

where H_0 is the mean sea level and $h(x)$ is the topographic ridge height, both constants.

To represent the dynamical effect of bottom drag, we follow the classic approach of Proudman, J. [11], integrating the horizontal momentum equation over the water column and parameterizing bottom stress using a quadratic drag law yields a frictional deceleration,

$$\frac{\partial \hat{u}}{\partial t} = -g\frac{\partial \eta}{\partial x} - \frac{k\,|\hat{u}|\,\hat{u}}{H} \tag{2}$$

where $\hat{u}(x,t)$ is the depth averaged along strait velocity, $\eta(x,t)$ is sea-surface height, k is seabed roughness.

Assume the bottom drag coefficient is linear, we linearize the quadratic drag about a rescaled velocity U_* within each constant height region, so that $|\hat{u}|\,\hat{u} \approx U_*\hat{u}$, therefore the effective linear drag coefficient is

$$\varepsilon(x) \equiv \frac{kU_*}{H(x)}, \tag{3}$$

which we treat as piecewise constant. The enhancement of drag can be interpreted as arising from larger roughness of bottom topography and/or larger velocity.

To simulate the Antarctic Circumpolar Current (ACC) through a narrow topographic constriction such as the Drake Passage, we work in a parameter regime where the drag in the shallow mountain strip is of order one, while the drag in the deeper basin is much smaller, which is

$$\varepsilon_2 = O(1) \quad \text{for } x \in [-x_0, 0], \qquad \varepsilon_1 \ll 1 \quad \text{for } x \in [0, L_x].$$

With the above setup, we define a barotropic streamfunction $\psi(x,y)$ satisfying a Stommel–type vorticity balance with sinusoidal wind–curl forcing $F(y)$,

$$F(y) = \frac{\tau_0 \pi}{L_y} \sin\left(\frac{\pi y}{L_y}\right), \tag{4}$$

where τ_0 is the amplitude of the zonal wind stress. Since $\varepsilon(x)$ is piecewise constant, the Stommel equation separates into two regions,

$$\beta\,\psi_x^{(j)} + \varepsilon_j \nabla^2 \psi^{(j)} = -\,F(y), \qquad j = 1, 2, \tag{5}$$

where β is the meridional gradient of the Coriolis parameter. Here $j = 1$ denotes the weak–drag basin region $x \in [0, L_x]$ with $\varepsilon_1 \ll 1$, and $j = 2$ denotes the mountain strip $x \in [-x_0, 0]$ with order–one drag ε_2, as sketched in the schematic domain in Figure 1. In the analysis that follows we will construct an explicit Stommel–type solution in region 2 and a Sverdrup–plus–boundary–layer solution in region 1, and then match them across the interfaces.

We impose Dirichlet boundary conditions in the meridional direction, $\psi^{(1,2)}(x,0) = C_2$ and $\psi^{(1,2)}(x,L_y) = C_1$, where C_1 and C_2 are specified values of the streamfunction at the northern and southern boundaries, their difference represents the total zonal mass flux through the channel. At the mountain edges $x = 0$ and $x = -x_0$, we require both continuity of the streamfunction,

$$[\psi] = 0,$$

and of the tangential stress,

$$[\varepsilon\psi_x] = 0,$$

where the brackets stand for jumps at the edges, $[a] = a^+ - a^-$. The continuity of ψ ensures mass conservation across the barrier, while the continuity of the tangential stress follows from conservation of meridional momentum.

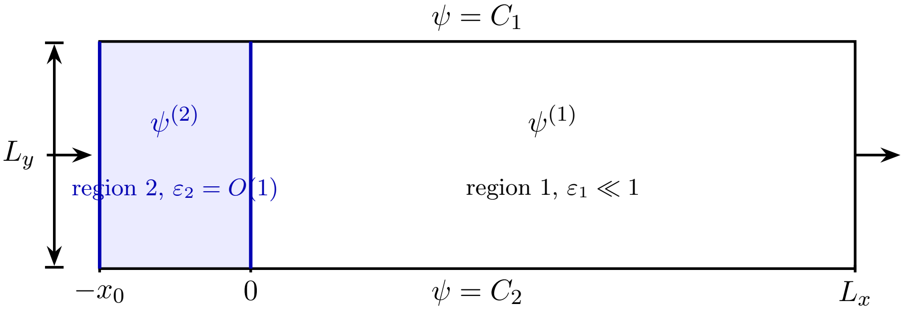

Figure 1: Schematic of the model domain $D = [-x_0, L_x] \times [0, L_y]$. The left strip $x \in [-x_0, 0]$ (shaded) represents a region with strong bottom drag $\varepsilon_2 = O(1)$, while the right part $x \in [0, L_x]$ (region 1) is a deeper basin with weak drag $\varepsilon_1 \ll 1$. The barotropic streamfunction is fixed to $\psi = C_2$ and $\psi = C_1$ at the southern and northern boundaries, respectively.

2.2 Explicit Solution

To simplify the boundary conditions in y, we subtract a background profile that already satisfies the Dirichlet values at $y = 0$ and $y = L_y$. In each region $j = 1, 2$, we write

$$\psi^{(j)}(x,y) = C_2 + (C_1 - C_2)\frac{y}{L_y} + \phi^{(j)}(x,y), \tag{6}$$

By construction, the background term $C_2 + (C_1 - C_2)y/L_y$ matches the prescribed values C_2 at $y = 0$ and C_1 at $y = L_y$, so the perturbation $\phi^{(j)}$ satisfies homogeneous Dirichlet conditions in y. Substituting into the Stommel's equation (5), we find that $\phi^{(j)}$ satisfies, in each region, the standard Stommel's model

$$\beta\,\phi^{(j)}_x + \epsilon_j\left(\phi^{(j)}_{xx} + \phi^{(j)}_{yy}\right) = -F(y). \tag{7}$$

We expand $\phi^{(2)}$ in a sine series in the meridional direction,

$$\phi^{(2)}(x,y) = \sum_{n=1}^{\infty} T^{(2)}_n(x)\,\sin(\kappa_n y), \quad \kappa_n = n\pi/L_y$$

which satisfies the boundary conditions automatically. Substituting this expansion into the equation for $\phi^{(2)}$ and using the orthogonality of the sine functions, we derive the following expression for each mode index m,

$$\varepsilon_j \left(T_m^{(2)}\right)'' + \beta \left(T_m^{(2)}\right)' - \varepsilon_j \kappa_m^2 T_m^{(2)} = -\frac{\tau_0 \pi}{L_y} \delta_{m1}, \tag{8}$$

where δ_{m1} is the Kronecker delta, since the wind–curl forcing (4) that we prescribe has the single–harmonic structure $F(y) \propto \sin\left(\frac{\pi y}{L_y}\right)$, corresponding exactly to $m = 1$. Consequently, only the $m = 1$ modal equation contains a nontrivial right–hand side; all modes with $m \geq 2$ satisfy homogeneous equations. For simplicity purpose, we will drop the mode index m in the following derivation.

In our model setup, we have adopted for simplicity a wind–curl forcing (4) containing only a single harmonic component. If the wind–stress curl exhibited a more complex meridional pattern—such as multiple jets, bands, or alternating wind systems—its expansion would involve several harmonics. In that case, each nontrivial coefficient F_m would act as a direct forcing term in the modal equation (8), producing a multi–mode response. The resulting flow field would be a superposition of all these forced modes.

To analyze the homogeneous part, we ansatz a solution in exponential form and obtain two real roots,

$$\lambda_{\pm}^{(2)} = \frac{-\beta \pm \sqrt{\beta^2 + 4\epsilon_2^2 \kappa_1^2}}{2\epsilon_2}.$$

The corresponding homogeneous solution in region 2 is therefore

$$T_h^{(2)}(x) = A^{(2)} e^{\lambda_+^{(2)} x} + B^{(2)} e^{\lambda_-^{(2)} x},$$

where coefficients $A^{(2)}$ and $B^{(2)}$ are to be determined from the jump conditions discussed in the model setup section.

For the inhomogeneous part, since the forcing does not depend on x, we seek a constant particular solution $T_p^{(2)}(x) = C^{(2)} = -\frac{\tau_0 L_y}{\epsilon_j \pi}$. Then the streamfunction in region 2 adopts the form

$$\phi^{(2)}(x, y) = \left[A^{(2)} e^{\lambda_+^{(2)} x} + B^{(2)} e^{\lambda_-^{(2)} x} + \frac{\tau_0 L_y}{\epsilon_2 \pi}\right] \sin\left(\frac{\pi y}{L_y}\right). \tag{9}$$

2.3 Sverdrup Transport and Boundary layer

In region 1, where the nondimensional bottom drag satisfies $\varepsilon_1 \ll 1$, we follow the standard Stommel construction and decompose the streamfunction into an interior (Sverdrup) solution plus a western boundary layer correction,

$$\phi^{(1)}(x, y) = \phi_{\text{outer}}^{(1)}(x, y) + \phi_{\text{inner}}^{(1)}(x, y) - \phi_{\text{intersec}}^{(1)}(x, y).$$

The outer solution $\phi_{\text{outer}}^{(1)}$ satisfies the leading-order Sverdrup balance, with $\varepsilon = 0$. Integration yields

$$\phi_{\text{outer}}^{(1)}(x, y) = \left(-\frac{\tau_0 \pi}{\beta L_y} x\right) \sin\left(\frac{\pi y}{L_y}\right) + B(y),$$

depending on an arbitrary function $B(y)$. For the boundary layer, we rescale x by ε, after which the solution to leading order yields

$$\phi_{\text{inner}}^{(1)} = A(y) e^{-\frac{\beta}{\epsilon_1} x} + C(y)$$

for arbitrary functions $A(y)$ and $C(y)$.

Because the forcing $F(y)$ is sinusoidal, the $A(y)$, $B(y)$, and $C(y)$ are proportional to $\sin(\frac{\pi y}{L_y})$, simplifying the functions into

$$A(y) = \hat{A}\sin(\frac{\pi y}{L_y}), \qquad B(y) = \hat{B}\sin(\frac{\pi y}{L_y}), \qquad C(y) = \hat{C}\sin(\frac{\pi y}{L_y}),$$

The matching condition between the inner and outer solution ($\phi^{(1)}_{\text{inner}}(+\infty, y) = \phi^{(1)}_{\text{outer}}(0, y)$) yields the intersection part

$$\phi^{(1)}_{\text{inner}}(+\infty, y) = \hat{C}\sin(\frac{\pi y}{L_y}) = \phi^{(1)}_{\text{outer}}(0, y) = \hat{B}\,\sin\left(\frac{\pi y}{L_y}\right),$$

which gives us the explicit solution in region (1)

$$\phi^{(1)} = \phi^{(1)}_{\text{outer}} + \phi^{(1)}_{\text{inner}} - \phi^{(1)}_{\text{intersec}} = \left(\hat{A}e^{-\beta x/\varepsilon_1} + \hat{B} - \frac{\tau_0 \pi}{\beta L_y}\,x\right)\sin\left(\frac{\pi y}{L_y}\right). \tag{10}$$

where $\hat{A}$, $\hat{B}$ are constants.

2.4 Boundary conditions

Applying the continuity conditions between the two regions discussed in Section 2.1, results in the following linear system,

$$\begin{pmatrix} 1 & 1 & -1 & -1 \\ e^{-\lambda_+^{(2)}x_0} & e^{-\lambda_-^{(2)}x_0} & 0 & -1 \\ \varepsilon_2\lambda_+^{(2)} & \varepsilon_2\lambda_-^{(2)} & \beta & 0 \\ \varepsilon_2\lambda_+^{(2)}e^{-\lambda_+^{(2)}x_0} & \varepsilon_2\lambda_-^{(2)}e^{-\lambda_-^{(2)}x_0} & 0 & 0 \end{pmatrix} \begin{pmatrix} A^{(2)} \\ B^{(2)} \\ \hat{A} \\ \hat{B} \end{pmatrix} = \begin{pmatrix} -\dfrac{\tau_0 L_y}{\varepsilon_2 \pi} \\ -\dfrac{\tau_0 L_y}{\varepsilon_2 \pi} - \dfrac{\tau_0 L_x}{\beta L_y} \\ 0 \\ -\dfrac{\tau_0}{\beta L_y} \end{pmatrix}. \tag{11}$$

A direct computation shows that $\det M \neq 0$, so the linear system (11) has a unique solution.

2.5 Background flow and streamfunction circulation ratio

The complete profile for region D is given by (6), where we now estimate the ratio between the background throughflow $(C_2 - C_1)$ and the characteristic circulation amplitude. For analytic simplification purpose, we assume density $\rho = 1$; then the barotropic steady linearized momentum equation in vector form is

$$-\mathbf{u}\cdot\nabla p + \boldsymbol{\tau}\cdot\mathbf{u} - \varepsilon|\mathbf{u}|^2 = 0,$$

integrate within the entire domain D and by the incompressibility and assumption of bottom drag to the leading order, we get

$$\iint_D \tau^x(\bar{U} - \phi_y^{(1,2)})\,dA \approx \iint_{[-x_0,0]\times[0,L_y]} \varepsilon_2\left[(\bar{U} - \phi_y^{(1,2)})^2 + {\phi_x^{(1,2)}}^2\right]dA,$$

which could be simplified and calculated out by the homogeneous boundary conditions into,

$$L L_y \bar{\tau}\,\bar{U} + \iint_D \tau_x'(y)\phi\, dA \approx \epsilon_2 x_0 L_y \bar{U}^2 + \epsilon_2 \iint_{\Omega_2} |\nabla\phi|^2\, dA.$$

We now estimate the two remaining integrals by introducing a characteristic amplitude Φ of the circulating streamfunction ϕ, and letting $\Delta\tau$ denote the meridional variation of the zonal wind stress. Then we can resulting the following scaling relation between the background streamfunction and the characteristic recirculating streamfunction

$$\frac{C_2 - C_1}{\Phi} \sim \frac{\bar{\tau}}{\Delta\tau}\left[\left(\frac{L_y}{x_0}\right)^2 + 1\right] := r, \tag{12}$$

where $r$is the background flow to circulation ratio. Applying the physical geometric parameters of the Drake Passage region and ERA5 based wind stress, this gives $r \approx 2.94$, which we use to reconstruct the $O(1)$ wind-driven circulation correction.

2.6 Wind-stress Parameter

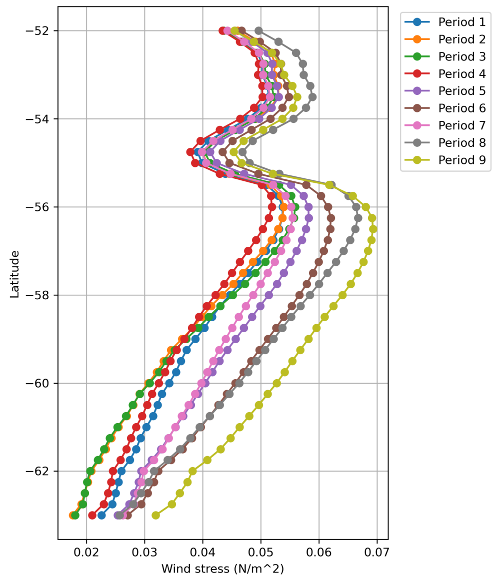

Figure 2: Ten-year zonal-average wind-stress.

To connect the idealized forcing in (4) to observations, we estimate the wind-stress parameters from monthly ERA5 near-surface winds over a Drake-Passage band from 1940 January first to 2025 December first [12]. Specifically, we use the 10 m wind components u_{10} and v_{10} on the latitude band $[-63°\text{S}, -52°\text{S}]$ and longitude band $[-70°\text{W}, -50°\text{W}]$. The wind stress is computed by the bulk aerodynamic formula

$$\boldsymbol{\tau} = (\tau_x, \tau_y) = \rho_a C_D \sqrt{u_{10}^2 + v_{10}^2}(\,u_{10}\,,\,v_{10}),$$

with air density $\rho_a = 1.225\ \mathrm{kg\,m^{-3}}$ and drag coefficient $C_D = 1.3 \times 10^{-3}$.

For each time t, we assume that the wind stress depends only on the meridional direction, and define the latitude-averaged wind stress $\overline{\tau}(\phi, t)$, where ϕ is the latitude, crossing the whole latitude domain. The full record is then divided into consecutive 10-year windows, and for each window W_k we compute the decadal-mean meridional profile $\overline{\tau}_k(\phi)$. From each decadal profile, we extract two scalar quantities, the latitude-mean stress $\tau_{\text{mean}}^{(k)}$ and meridional wind stress variation $\Delta\tau^{(k)}$.

Figure 2 shows that the ERA5-derived decadal zonal-mean stress profiles $(\overline{\tau}(\phi, t))$ are not sinusoidal. However, the dominant meridional variation is smooth and large-scale, with a broad southern minimum, an interior maximum, and a gradual transition between them. This supports the use of a single sinusoidal mode as a first-order approximation in our analytic model.

The residual comes from having multiple jets, asymmetry in latitude, and other local features of the actual Southern Atlantic wind field. In a more general version of the model, these deviations could be incorporated by expanding the forcing in multiple meridional modes, producing a superposition of the corresponding streamfunction responses.

3 Discussion

The Drake Passage is a narrow, topographically rough sector of the Antarctic Circumpolar Current (ACC) where steep ridges and fracture zones generate strong bottom–pressure (form) stresses; in this sector, analyses and state estimates consistently indicate that the large-scale wind forcing on the mean flow is closed predominantly by form stress over bathymetry, with only a small residual requiring viscous dissipation [13]. This motivates our representation of Drake Passage as a zone of enhanced effective bottom drag adjacent to a weak–drag basin, offering a simple barotropic idealization that isolates how localized dissipation can redirect wind-driven transport [9].

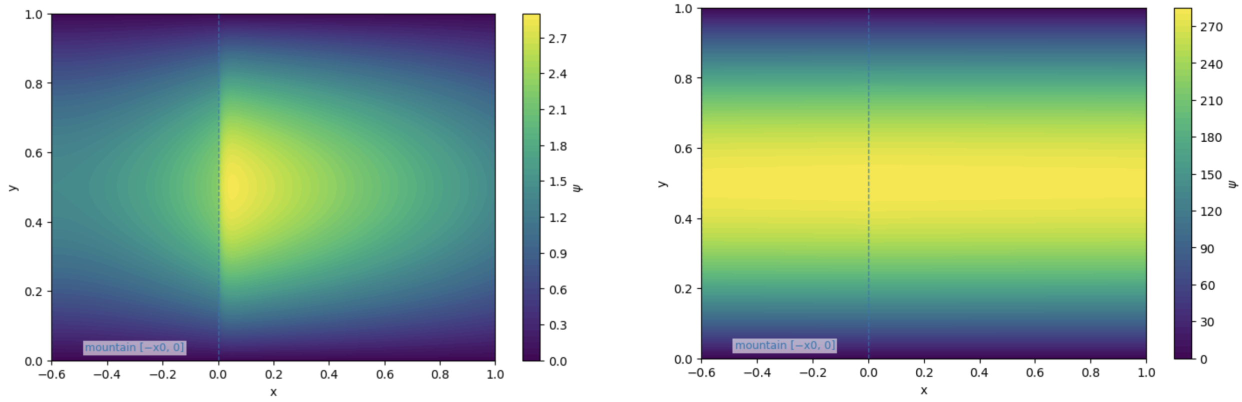

(a) High-drag passage ($\varepsilon_1 = 0.003$, $\varepsilon_2 = 0.5$)

(b) Uniform-drag control ($\varepsilon_1 = \varepsilon_2 = 0.003$)

Figure 3: Effect of drag heterogeneity on the wind-driven circulation.

When the drag contrast is large ($\mathcal{O}(1) \sim \varepsilon_2 \gg \varepsilon_1$), the streamfunction develops a sharp meridional shear at the eastern edge of the ridge ($x = 0$), producing the northward branch (Figure 3a). In our high-drag simulation (Figure 3a), we set $\varepsilon_1 = 0.003$ in the weak-drag basin and $\varepsilon_2 = 0.5$ in the “passage” strip to represent enhanced bottom drag over the Drake Passage, nondimensional planetary vorticity gradient $\beta = 2.0$, nondimensional wind stress curl amplitude $\tau_0 = 1.0$, and no imposed barotropic background flow $C_1 = C_2 = 0$, so any throughflow arises from the wind/topography balance.

Figure 3b serves as a comparison case. When the drag is the same on both sides of the ridge $\varepsilon_1 = \varepsilon_2 = 0.003$ and keep other parameters unchanged, the interface no longer supports a jump crossing $x = 0$, yielding an unbounded zonal Sverdrup pattern with negligible meridional flow. The two figures illustrate that a narrow, high-drag passage is sufficient to rotate a portion of the wind-driven transport meridionally, even without invoking baroclinicity or time dependence.

Comparing Figure 3a and Figure 3b, we find that decreasing the bottom drag coefficient in region 2 by $\mathcal{O}(10^2)$ leads to an $\mathcal{O}(10^2)$ increase in the streamfunction amplitude. This scaling matches the analytic solution: in equation (9), the wind-forced contribution has a prefactor proportional to $\tau_0 L_y/(\varepsilon_2 \pi)$, keeping τ_0 and L_y fixed implies $\psi \sim \varepsilon_2^{-1}$, so reducing ε_2 by a factor of 10^2 amplifies the wind-driven streamfunction by the same factor.

Incorporating the first order magnitude estimation of the streamfunction (6), Drake Passage geometric parameters, and the ERA5-based wind-stress scales, gives a nondimensional ratio of streamfunction circulation and background flow ratio r about $r \approx 2.94$. The reconstructed field shows that the effect of the Drake Passage is not to replace the large-scale throughflow, but to perform a local deformation of this flow. In nondimensional coordinates, the added background profile imposes the dominant basin-scale meridional gradient, while the circulation correction preserves the localized distortion generated by drag heterogeneity near the interface $x = 0$. Thus the sharp shear associated with the high-drag strip remains visible, appearing as an $O(1)$ perturbation embedded in the ACC throughflow. The reconstructed solution (6) is mapped back into dimensional region zoomed in longitude-latitude coordinates in Figure 4b, the resulting pattern provides a more direct Drake-Passage interpretation. Figure 5b shows the velocity field superimposed on the streamfunction contours in the same domain, with arrow color indicating the nondimensional speed magnitude. Away from the Drake Passage, the flow remains predominantly zonal, consistent with the large-scale ACC-like throughflow. In contrast, near the eastern edge of Drake Passage and in the immediately downstream region (highlighted by the yellow shaded strip), the velocity vectors develop a northward component. This indicates that, after exiting the passage, part of the flow turns northward.

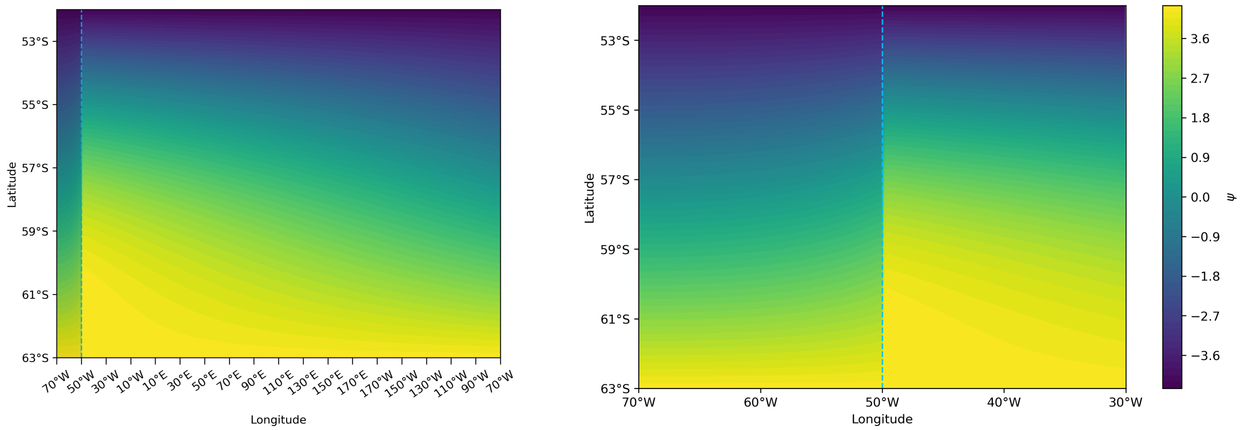

(a) Streamfunction contours

(b) Drake Passage sector

Figure 4: Reconstructed total streamfunction

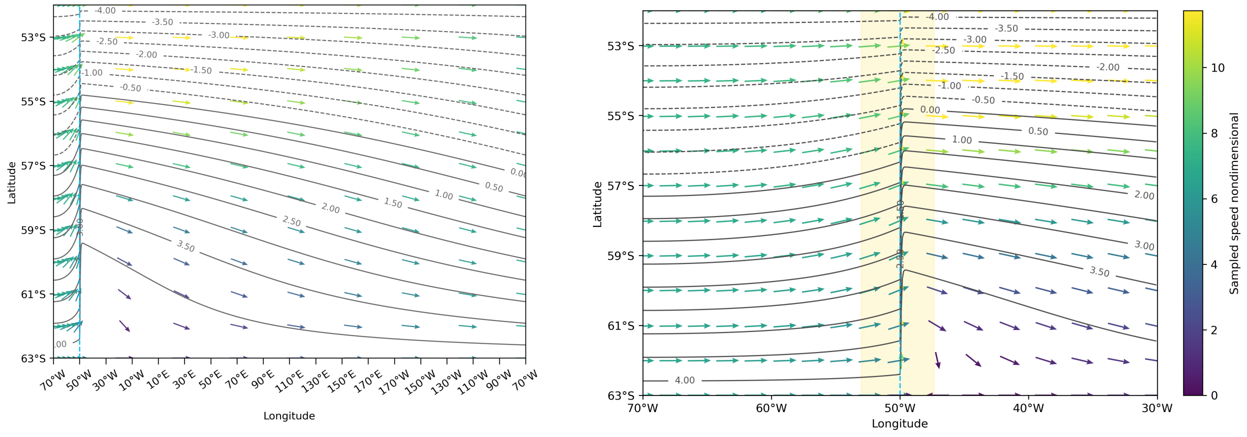

(a) velocity field

(b) Drake Passage velocity field

Figure 5: Reconstructed velocity field

In the mapped longitude-latitude view, this localized northward branch is the model analogue of a Malvinas Current-like feature. As a consequence, the downstream flow is much stronger in the northern part of the connection region than in the southern part[14], a pattern qualitatively consistent with observational and reanalysis-based descriptions of the Malvinas Current and the transfer of ACC waters into the western South Atlantic [15].

Our present solution fixes the northern and southern boundaries at constant streamfunction, which is convenient analytically but unrealistic for the ACC sector. The northern and southern edges of a Drake–Passage sector are dynamically open. Observations show that the ACC transport through Drake Passage varies substantially in time and with depth: the cDrake moored array reported a full–depth mean of 173.3 ± 10.7 Sv (decomposed into a barotropic 45.6 ± 8.9 Sv plus baroclinic 127.7 Sv component) [16], whereas other programs synthesize values near ~ 141 Sv [5]. Along the northern flank, the Malvinas Current—the northward branch fed by the ACC—carries a section–dependent transport that decreases from ~ 40 Sv at 51°S to ~ 35 Sv at 41°S in the upper ~ 900 m [14]; sustained estimates at 41°S give a mean of 37.1 ± 2.6 Sv with interannual standard deviation of order 6–7 Sv [17]. Together these results require varies at the northern and southern edges, rather than fixed–ψ conditions.

4 Conclusion

This article has developed a simple barotropic model for wind–driven circulation in a zonally unbounded channel with a narrow region of enhanced bottom drag, extending the classical Stommel's framework [1] for closed basins to a configuration motivated by the ACC flowing through Drake Passage. Constructing an explicit solution in the high–drag passage and a Sverdrup–plus–boundary–layer solution in the weak–drag basin, and matching them across the interfaces, yields a fully analytic description of how localized dissipation redirects the wind–driven transport.

Our results estimate gives a background flow to circulation flow ratio about $r \approx 2.94$, so the localized circulation remains an $O(1)$ deformation embedded within a larger zonal through flow, which regionally modifies the background zonal flow, consistent with the sharp lateral velocity gradients observed in the Malvinas Current [14]. In contrast, when drag is uniform on both sides of the ridge, the flow relaxes to a nearly zonal Sverdrup pattern with negligible meridional transport. This comparison demonstrates that a finite, localized enhancement of bottom drag is sufficient, in a purely barotropic setting, to rotate a portion of the wind–driven transport from zonal to meridional without invoking baroclinicity, time dependence, or explicitly resolved mesoscale eddies. In this sense, the model provides a minimal, fully analytic analogue to more complex numerical studies of the ACC that include form stress and topographic control.

At the same time, the model makes several idealizations that point directly to future work. The representation of topographic control through a piecewise-constant drag artificially closes the meridional boundaries with fixed streamfunction. In reality, the northern and southern edges of a Drake–Passage sector are dynamically open in both depth and time, with variable inflow and outflow that communicate with the Scotia Sea, the western South Atlantic (including the Argentine Basin), and the southeast Pacific sectors of the ACC [18–20]. A natural next step is therefore to replace Dirichlet conditions with more realistic transport or radiation conditions that permits the circumpolar exchange and investigate how localized drag interacts with the prescribed net circumpolar transport. Incorporating baroclinic structure and simple parameterizations of form stress into the present framework would allow a closer comparison with eddy–resolving models and observations of ACC transport partition between barotropic and baroclinic components, and embedding this high–drag passage and weak–drag basin into a larger multi–gyre configuration would help clarify how localized topographic control in Drake–Passage–like sectors feeds boundary currents and western boundary systems in adjacent basins.

References

[1] Henry Stommel. The westward intensification of wind-driven ocean currents. *Eos, Transactions American Geophysical Union*, 29(2):202–206, 1948.

[2] Joseph Pedlosky. *Geophysical fluid dynamics*. Springer Science & Business Media, 2013.

[3] SA Cunningham, SG Alderson, BA King, and MA Brandon. Transport and variability of the antarctic circumpolar current in drake passage. *Journal of Geophysical Research: Oceans*, 108 (C5), 2003.

[4] Zoé Koenig, Christine Provost, Ramiro Ferrari, Nathalie Sennéchael, and Marie-Hélène Rio. Volume transport of the a ntarctic c ircumpolar c urrent: Production and validation of a 20 year long time series obtained from in situ and satellite observations. *Journal of Geophysical Research: Oceans*, 119(8):5407–5433, 2014.

[5] Xiaobiao Xu, Eric P Chassignet, Yvonne L Firing, and Kathleen Donohue. Antarctic circumpolar current transport through drake passage: What can we learn from comparing high-resolution model results to observations? *Journal of Geophysical Research: Oceans*, 125(7): e2020JC016365, 2020.

[6] Alejandro H Orsi, Thomas Whitworth III, and Worth D Nowlin Jr. On the meridional extent and fronts of the antarctic circumpolar current. *Deep Sea Research Part I: Oceanographic Research Papers*, 42(5):641–673, 1995.

[7] Serguei Sokolov and Stephen R Rintoul. Circumpolar structure and distribution of the antarctic circumpolar current fronts: 1. mean circumpolar paths. *Journal of Geophysical Research: Oceans*, 114(C11), 2009.

[8] L St. Laurent, Alberto C Naveira Garabato, James R Ledwell, Andreas M Thurnherr, John M Toole, and Andrew J Watson. Turbulence and diapycnal mixing in drake passage. *Journal of Physical Oceanography*, 42(12):2143–2152, 2012.

[9] Matthew R Mazloff, Patrick Heimbach, and Carl Wunsch. An eddy-permitting southern ocean state estimate. *Journal of Physical Oceanography*, 40(5):880–899, 2010.

[10] Yue Bai, Yan Wang, and Andrew L Stewart. Does topographic form stress impede prograde ocean currents? *Journal of Physical Oceanography*, 51(8):2617–2638, 2021.

[11] Joseph Proudman. Dynamical oceanography. *(No Title)*, 1953.

[12] Hans Hersbach, Bill Bell, Paul Berrisford, Shoji Hirahara, András Horányi, Joaquín Muñoz-Sabater, Julien Nicolas, Carole Peubey, Raluca Radu, Dinand Schepers, et al. The era5 global reanalysis. *Quarterly journal of the royal meteorological society*, 146(730):1999–2049, 2020.

[13] Dirk Olbers, DANIEL Borowski, Christoph Völker, and Jorg-Olaf Wölff. The dynamical balance, transport and circulation of the antarctic circumpolar current. *Antarctic science*, 16(4): 439–470, 2004.

[14] DI Frey, Alberto Ricardo Piola, VA Krechik, DV Fofanov, EG Morozov, KP Silvestrova, R Yu Tarakanov, and SV Gladyshev. Direct measurements of the malvinas current velocity structure. *Journal of Geophysical Research: Oceans*, 126(4):e2020JC016727, 2021.

[15] Camila Artana, Christine Provost, Lea Poli, Ramiro Ferrari, and Jean-Michel Lellouche. Revisiting the malvinas current upper circulation and water masses using a high-resolution ocean reanalysis. *Journal of Geophysical Research: Oceans*, 126(6):e2021JC017271, 2021.

[16] Kathleen A Donohue, KL Tracey, D Randolph Watts, María Paz Chidichimo, and TK Chereskin. Mean antarctic circumpolar current transport measured in drake passage. *Geophysical Research Letters*, 43(22):11–760, 2016.

[17] Camila Artana, Ramiro Ferrari, Zoé Koenig, Nathalie Sennéchael, Martin Saraceno, Alberto R Piola, and Christine Provost. Malvinas current volume transport at 41 s: A 24 yearlong time series consistent with mooring data from 3 decades and satellite altimetry. *Journal of Geophysical Research: Oceans*, 123(1):378–398, 2018.

[18] Yann Friocourt, Sybren Drijfhout, Bruno Blanke, and Sabrina Speich. Water mass export from drake passage to the atlantic, indian, and pacific oceans: a lagrangian model analysis. *Journal of physical oceanography*, 35(7):1206–1222, 2005.

[19] Dhruv Balwada, Kevin G Speer, Joseph H LaCasce, W Brechner Owens, John Marshall, and Raffaele Ferrari. Circulation and stirring in the southeast pacific ocean and the scotia sea sectors of the antarctic circumpolar current. *Journal of Physical Oceanography*, 46(7):2005–2027, 2016.

[20] Anna Olivé Abelló, Josep L Pelegrí, Francisco J Machín, and Ignasi Vallès-Casanova. The transfer of antarctic circumpolar waters to the western south atlantic ocean. *Journal of Geophysical Research: Oceans*, 126(7):e2020JC017025, 2021.